*Solar RRL*

WILEY VCH

Solar RRL

RESEARCH ARTICLE OPEN ACCESS

# Outdoor Performance and Thermally Accelerated Degradation of Inverted Perovskite Solar Cells

Ryousuke Ishikawa[1,2] | Hayato Okawa[1] | Masatoshi Yanagida[3] | Yasuhiro Shirai[3] | Makoto Konagai[2]

[1]Department of Electrical, Electronic and Communication Engineering, Tokyo City University, Setagaya-ku, Japan | [2]Advanced Research Laboratories, Tokyo City University, Setagaya-ku, Japan | [3]Photovoltaic Materials Group, Center for GREEN Research on Energy and Environmental Materials, National Institute for Materials Science (NIMS), Tsukuba, Japan

**Correspondence:** Makoto Konagai (mkonagai@tcu.ac.jp)

**Received:** 6 July 2025 | **Revised:** 16 September 2025 | **Accepted:** 28 September 2025

**Funding:** Priority Research Project of Tokyo City University

**Keywords:** outdoor performance | perovskite solar cells | thermal phase transition

## ABSTRACT

In this article, the long-term outdoor performance of inverted perovskite solar cells (PSCs) with glass–glass encapsulation is investigated over a 3-year period. Despite achieving initial power conversion efficiencies of >20%, the devices show significant degradation during summer months, particularly when surface temperatures exceed 50°C, with their internal cell temperatures increasing to ~90°C. Optical and scanning electron microscopy imaging reveal the formation of a high-resistance phase within the perovskite layer, particularly near the $NiO_x$ interface, as the major degradation pathway. Indoor accelerated tests, conducted under heat and light conditions, replicate these effects, indicating the occurrence of thermally induced phase transitions. The measurement methodology also influences the degradation; devices measured with maximum power point tracking show slightly less deterioration than do those assessed via current–voltage curve tracing. Additionally, UV-cut filters show minimal benefits, likely owing to the inherent UV blocking feature of $NiO_x$. These findings underscore the critical role of thermal management and operational conditions in ensuring the stability of PSCs. Further improving the material design, encapsulation, and measurement protocols is essential for enhancing the outdoor reliability and commercial viability of PSCs.

## 1 | Introduction

Perovskite solar cells (PSCs) have garnered considerable attention in recent years because of their rapidly advancing power conversion efficiencies, facile fabrication processes, and potential for low-cost lightweight photovoltaic applications. Laboratory-scale devices have achieved efficiencies exceeding 25%, which are comparable to those of conventional silicon-based solar cells [1–3]. Among the various device architectures, the inverted (p–i–n) structure has gained interest owing to its compatibility with flexible substrates and reduced hysteresis behavior [4–6].

Despite their promising attributes, the practical deployment of PSCs in outdoor environments remains a significant challenge. Notably, the long-term stability of perovskite materials under real-world operating conditions, including variable temperatures, humidities, solar irradiation, and electrical loads, has not yet been systematically and comprehensively examined. Although numerous studies on PSC degradation under controlled indoor conditions have been reported to date [7–11], its long-term behavior in actual outdoor environments remains underexplored [12–15].

Outdoor degradation of PSCs is primarily driven by temperature fluctuations, UV exposure, and electrochemical stress, which lead to failure modes such as ion migration, film cracking, and interface degradation [11, 16]. High operating temperatures, often exceeding 80°C during peak sunlight hours,

reportedly accelerate the degradation of the perovskite layer, resulting in significant efficiency losses [12]. Previous studies demonstrate that high-temperature stress can induce the formation of low-conductivity phases within perovskite materials, thereby contributing to their long-term performance deterioration [17–19].

In this study, we investigated the outdoor stability of encapsulated PSCs with an inverted architecture: glass/indium–tin oxide (ITO)/$NiO_x$/perovskite/$C_{60}$/bathocuproine (BCP)/Ag. We performed multiyear outdoor monitoring under different installation configurations and conducted a comparative analysis based on accelerated indoor degradation tests to identify the key degradation pathways. We specifically focused on the impact of high temperatures, UV exposure, and measurement methodologies (current–voltage (*I–V*) curve tracing vs. maximum power point tracking (MPPT)) on the long-term performance of PSC devices.

Our findings demonstrated that high cell temperatures, which frequently exceeded 80°C during the summer within the study period, play a critical role in inducing resistive phases within the perovskite layer and thus lead to substantial efficiency losses. Comparable degradation features were reproduced under controlled indoor heating and illumination conditions, suggesting that thermally driven phase transitions, potentially coupled with charge accumulation, were central to the observed degradation mechanisms. The investigated correlation between the outdoor and indoor degradation behaviors provides insights into PSC reliability under realistic operating conditions. These findings highlight the necessity for developing effective thermal management and measurement protocols to achieve long-term stability in perovskite photovoltaics.

## 2 | Results and Discussion

### 2.1 | Long-Term Outdoor Degradation Behavior

Figure 1 illustrates the degradation trend of the devices over 3 years. The initial efficiencies ranged from 20% to 23% (Figure S1 and Table S1), and all the devices exhibited notable degradation during the summer. New samples, measured in April 2023 using a four-terminal configuration, showed initial efficiencies of >20% and fill factors of ~0.8. A significant performance loss was observed in July 2023 and August 2023. The samples subjected to two-axis tracking exhibited an earlier onset of degradation than did those with a fixed-tilt configuration.

To assess the impact of UV light, the devices were exposed to outdoor conditions with and without UV-cut filters (cut-off < 400 nm). The quantum efficiency (QE) spectrum of the filter is presented in Figures 2a, and 2b shows the daily efficiency degradation as a function of accumulated solar exposure. The negligible effect of the UV filter may be attributed to the UV transmittance of $NiO_x$. The transmittance spectra shown in Figure S2 indicate that ~20 nm-thick $NiO_x$ blocks approximately 10% of UV light (wavelength <400 nm) [20].

### 2.2 | Comparison between *I–V* Curve Tracing and MPPT

Beginning in April 2024, MPPT measurements were conducted alongside *I–V* curve tracing owing to concerns that *I–V* curve tracing may contribute to degradation. Figure 3 compares the MPPT measurement and *I–V* curve tracing results. The MPPT measurements continuously tracked the maximum power point,

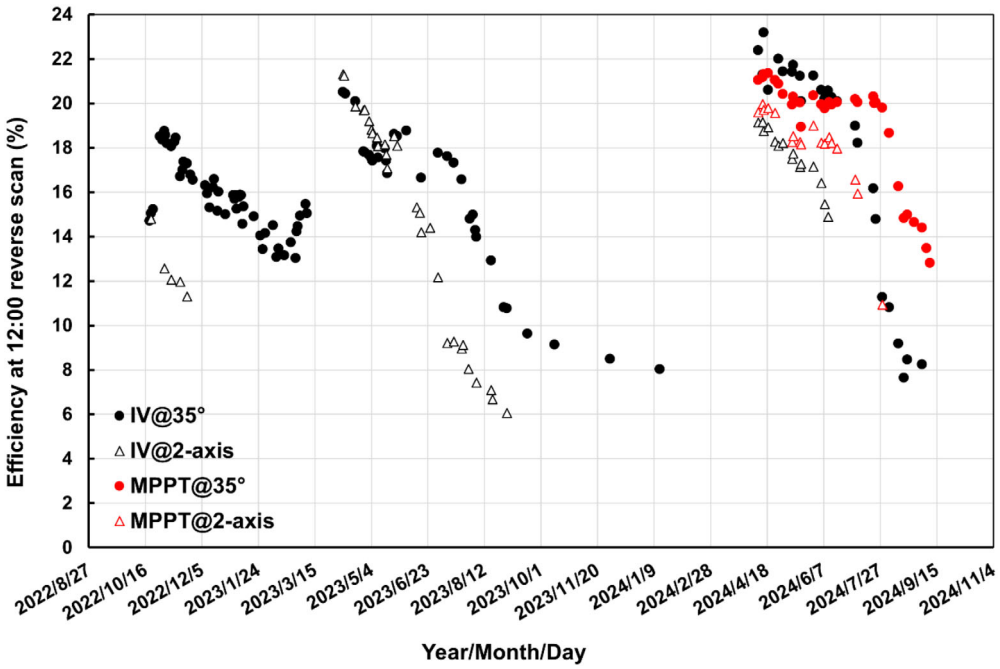


**FIGURE 1** | Long-term outdoor degradation trend.

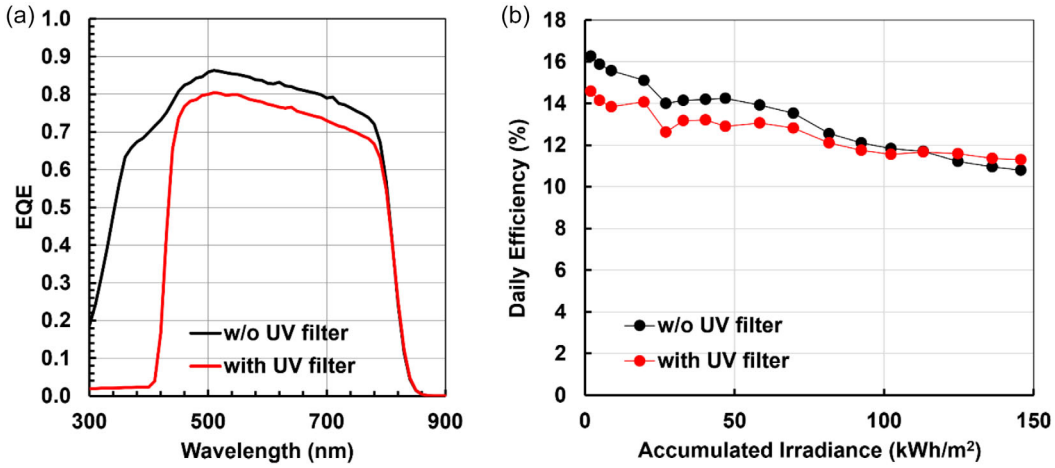


**FIGURE 2** | (a) QE spectrum and (b) daily efficiency degradation of PSC with the UV filter.

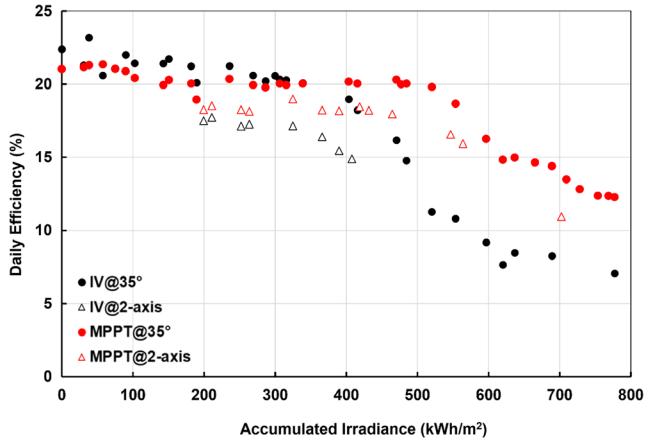


**FIGURE 3** | Daily efficiency degradation due to MPPT and *I–V* curve tracing measurements.

whereas, the *I–V* curves were measured only three times daily at 11:00, 12:00, and 13:00 JST. The daily average efficiency (defined as the total amount of electricity generated per day divided by the accumulated solar radiation on the same day) data were plotted only for days with solar irradiance greater than 5 kWh/m$^2$. Although the number of samples was limited, the MPPT resulted in slightly less degradation than did the *I–V* curve tracing method. The *I–V* measurements were performed in an open state; therefore, the behavior of the carriers inside the cell was different from that revealed by the MPPT method [21]. Moreover, the cell temperatures were possibly different.

## 2.3 | Temperature Dependance

Figure 4 compares the temperature and conversion efficiency measured at 12:00 using the *I–V* curve tracing method for the south-facing tilt angle of 35°. The temperature trend shows the surface temperature at 12:00 and the instantaneous maximum temperature of the day (Figure 4a). The conversion efficiency data are plotted for an irradiation intensity of approximately 100 mW/cm$^2$ at 12:00 h (Figure 4b). For PSCs, a large fill factor is observed under low irradiation intensities, even after degradation. A comparison of the data collected under meteorological conditions, with irradiation intensities above a certain threshold, reveals that both the methods yield similar results. The examined trends of $R_{sh}$ and $R_s$, shown in Figure S3, indicate that in late July, $R_s$ increases, while $R_{sh}$ decreases sharply, concurrent with the increase in temperatures.

The data indicated that conversion efficiency and fill factors gradually degraded from April 2024, with rapid degradation occurring when the surface temperature exceeded 50°C in July and August 2024. Furthermore, the initially minimal hysteresis gradually increased. When no temperature correction was applied to the solar cells, the conversion efficiency decreased from its initial value of 20% to 10%–15% by the end of August 2024.

Organic-halide perovskite materials are highly susceptible to moisture, humidity, temperature, and solar radiation, which significantly affect the degradation process. Figure S4 compares the humidity data for the same period shown in Figure 4. The humidity data are plotted as the average and maximum daily humidity measured using a hygrometer installed at the same location as that of the solar cell. Because temperature and humidity are correlated to Tokyo's climate, a strong correlation is expected between performance degradation and humidity. However, no distinct change in the humidity was observed during the periods of accelerated degradation. Furthermore, the encapsulated cells used in this study maintained an initial efficiency of 88.48% after 1000 h of continuous irradiation at 1 sun in an MPPT environment with $T = 60$°C and $RH = 30\%–35\%$ (as shown in by Khadka et al. [6]). These factors demonstrate the negligible effect of moisture penetration on the rapid degradation modes of these devices.

## 2.4 | Estimation of Cell Temperature

To estimate the internal cell temperature, the open-circuit voltage ($V_{oc}$) was analyzed as a function of the surface temperature of the devices (Figure S5). The thermal coefficient was $\Delta V_{oc} = -1.8 \frac{mV}{°C}$, which was consistent with reported values [12, 22].

In this study, the sample was sealed with glass, and the whole system was solidified with resin and adhesive; therefore, the final

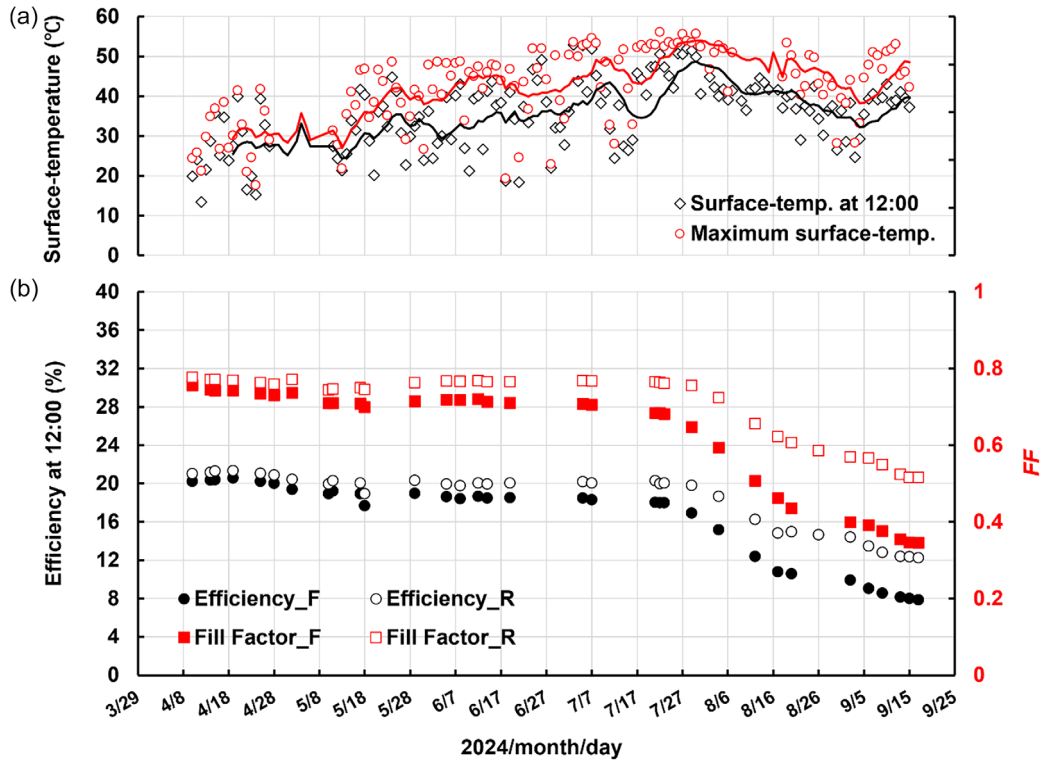


**FIGURE 4** | Comparison of (a) temperature and (b) efficiency degradation.

structure was extremely prone to heat buildup. In other words, a large discrepancy was expected between the measured surface temperature and actual 'cell temperature' at the junction. Therefore, in outdoor measurements, we estimated the 'cell temperature' at high temperatures from the $I_{sc}$–$V_{oc}$ measurement results obtained on a sunny day [23]. Figure 5 shows that the $V_{OC}$ values for the 35° sample and for the sample with two-axis tracking shift by 60 and 100 mV, respectively, which correspond to temperature increments of 33 and 56°C (determined by converting the temperature characteristic results into temperature values), respectively. This result suggests that the cell temperature increases to ~90°C during the hot summer months.

## 2.5 | Microscopic and Structural Changes

Optical microscopy (OM) images revealed a localized contrast change for the sample deteriorated outdoors (Figure 6b). The ratio of spots with different contrasts in the OM images was quantified; more areas with a high contrast in the image yielded a higher 'Mean.Value.' For example, the Mean.Value changed from 17.84 to 29.62 before and after outdoor exposure (Figure 6a and 6b), respectively. In addition, scanning electron microscopy (SEM) visualization of the cross-section of this sample revealed the presence of a highly resistive phase in the perovskite layer (Figure 7). When the same field of view was observed

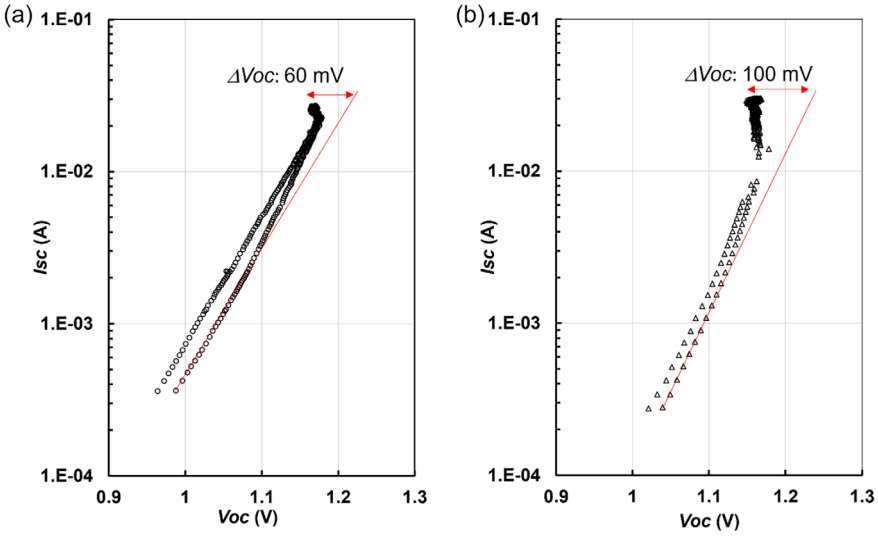


**FIGURE 5** | $I_{sc}$–$V_{oc}$ plots of the (a) 35° and (b) two-axis tracking samples.

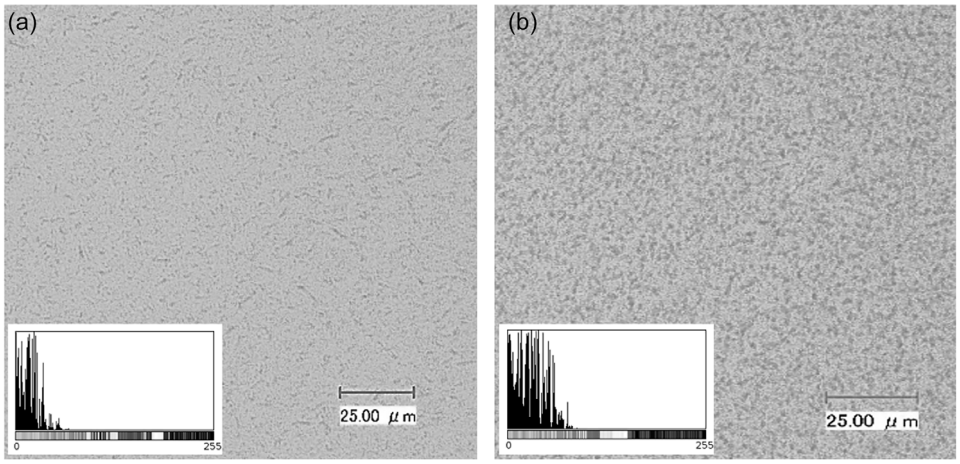


**FIGURE 6** | OM images of the (a) initial and (b) outdoor-degraded samples.

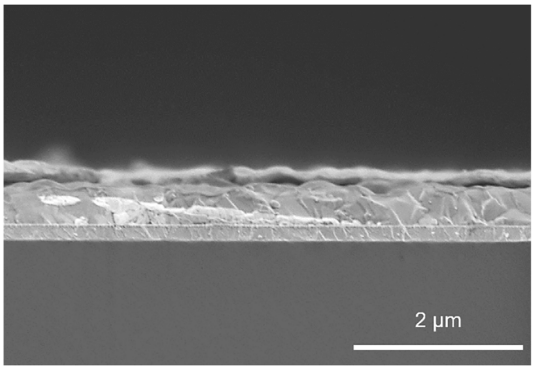


**FIGURE 7** | Cross-sectional image of the outdoor-degraded sample.

at a high magnification, an increase in the emission current density was detected. Therefore, the highly resistive phase was charged and appeared bright owing to the surface-charge effect (Figure S6). This phase appeared on the light-irradiated hole-transport-layer side; no such phase detected on the back side that contained the Ag electrode. Although the reaction between the metal electrode and halogen is one of the factors of deterioration [11], the results obtained in our study indicate the heat-induced phase transition as the primary degradation mechanism of or samples.

To corroborate this degradation mechanism, we used a sealed, unexposed sample heated on a hot plate under light irradiation in an indoor solar simulator to reproduce outdoor degradation. After heating for 24 h on a hot plate at 70°C under 1 sun irradiation in air, spots were observed under an optical microscope (Mean.Value = 25.79; Figure 8a). In addition, cross-sectional SEM images revealed the presence of a high-resistance phase in the perovskite layer similar to that observed in the outdoor-degraded sample (Figure 8b). Table 1 summarizes the results obtained by heating with and without light irradiation under open-circuit and short-circuit conditions (Figure S7), providing insights into the effects of various parameters. Evidently, a high-resistance phase was observed in all the heated samples. The ratio of spots under an optical microscope varied as: dark/open < light/open < dark/short << light/short. This result suggests that this mode of degradation is affected by—temperature,

**TABLE 1** | Summary of indoor testing.

| | Indoor | | | | Outdoor |
|---|---|---|---|---|---|
| Heat | 70°C | | | | up to 90°C |
| Light | w/o | w/o | 1 sun | 1sun | up to 1.2 sun |
| Circuit | open | short | open | short | IV tracing |
| SEM (Phase Change) | ✓ | ✓ | ✓ | ✓ | ✓ |
| OM (Mean. Value) | 14.57 | 17.65 | 16.18 | 25.79 | 29.62 |

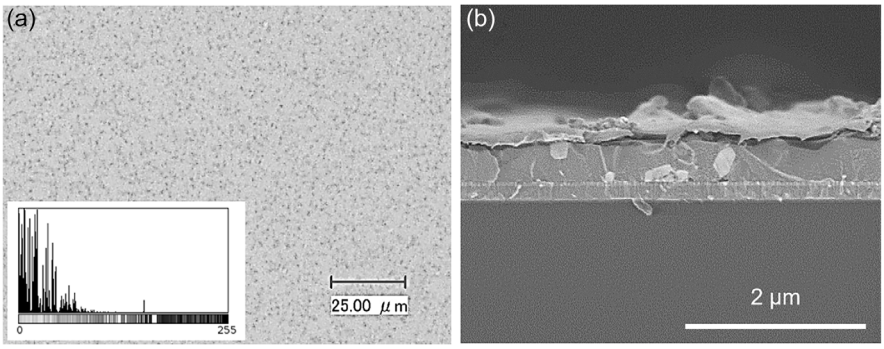


**FIGURE 8** | (a) OM and (b) cross-sectional SEM images of the indoor-treated samples.

light, and the flow of electrons. This high-resistance phase may be indexed as the δ phase that transforms from the $\alpha$ phase. However, no δ-phase diffraction peak was visible in the X-ray diffraction (XRD) profiles of the degraded samples (Figure S8). This absence of δ-phase diffraction peaks may be attributed to the low volume ratio or low crystallinity of these high-resistance phases. Analytical methods, such as transmission electron microscope (TEM) diffraction, for detecting crystallographic high-resistance phases in minute areas will be discussed in the future.

## 3 | Conclusion

In this study, we investigated the long-term outdoor performance and degradation mechanisms of inverted-structure PSCs over a 3-year period. The results revealed significant efficiency losses, particularly during the summer months; these losses were correlated with the increased surface temperatures that exceeded 50°C, and the estimated cell temperature occasionally approached 90°C. This thermal stress led to the formation of a high-resistance phase within the perovskite layer, primarily on the $NiO_x$ side (confirmed by OM and cross-sectional SEM observations). A comparative analysis of the *I–V* curve tracing and MPPT measurements suggested that compared to the former, the MPPT method resulted in slightly less degradation, potentially owing to reduced thermal or electrical stress. The reproduction of the degradation phenomena under controlled indoor heating and illumination conditions confirmed that thermal and photo-induced stress, combined with charge carrier flow, accelerated the formation of high-resistance regions. To prevent such phase transitions, the $NiO_x$ surface can be modified by a more stable treatment [24, 25] or by incorporating trivalent cation species into the B sites [26].

Overall, our findings emphasize the importance of thermal management for achieving long-term stability of PSCs, particularly under real-world outdoor conditions. Future investigations should be focused on improving the thermal stability through material engineering and module design to suppress heat-induced phase transitions and extend the operational lifetime of PSCs.

## 4 | Experimental Methods

### 4.1 | Device Fabrication

Inverted structured glass/ITO/$NiO_x$/perovskite/$C_{60}$/BCP/Ag PSCs that were used for the outdoor measurements were fabricated at the National Institute for Materials Science, Japan. The $NiO_x$ surface was treated with MeO-2PACz, and the MA/Br-free perovskite layer was passivated with piperazine dihydride. Detailed information on the fabricated PSCs is reported elsewhere [6, 27]. Devices were prepared on 5 $cm^2$ substrates containing four individual cells, each with a light-receiving area of 1.26 $cm^2$. The cells were encapsulated on both sides using glass and epoxy resins. For outdoor deployment, copper wires were soldered to the electrodes, followed by secondary sealing using a resin and adhesive (Figure 9).

### 4.2 | Indoor Testing

The initial and postdegradation device performances were characterized by QE measurements (Bunkokeiki CEP-25NLT) and under simulated AM1.5 solar illumination (EKO Instruments). For QE and current density–voltage (*J–V*) characterization, a 1-$cm^2$ shadow mask was applied, and all the measurements were performed at a controlled temperature of 25°C. The indoor durability testing of the sealed cells conformed to ISOS-L L2 or L3 (as reported by Khadka et al. [6]). Accelerated degradation tests were conducted using a solar simulator and with substrate heating. Heating the cells to approximately 70°C successfully reproduced the degradation behavior observed under outdoor conditions. The surface and cross-sectional morphologies were analyzed using OM (KEYENCE VHX-500F) and field-emission SEM (HITACHI SU3480). Crystal structure analysis was conducted using thin-film XRD (Bruker AXS D8 Discover) with a grazing incidence angle of 1.2° and a 2$\theta$ scan range of 10°–50°. Prior to the XRD measurements, the Ag electrode was removed using Kapton tape.

### 4.3 | Outdoor Testing

The outdoor performance was evaluated using two installation methods: a fixed south-facing tilt at 35° and a two-axis tracking

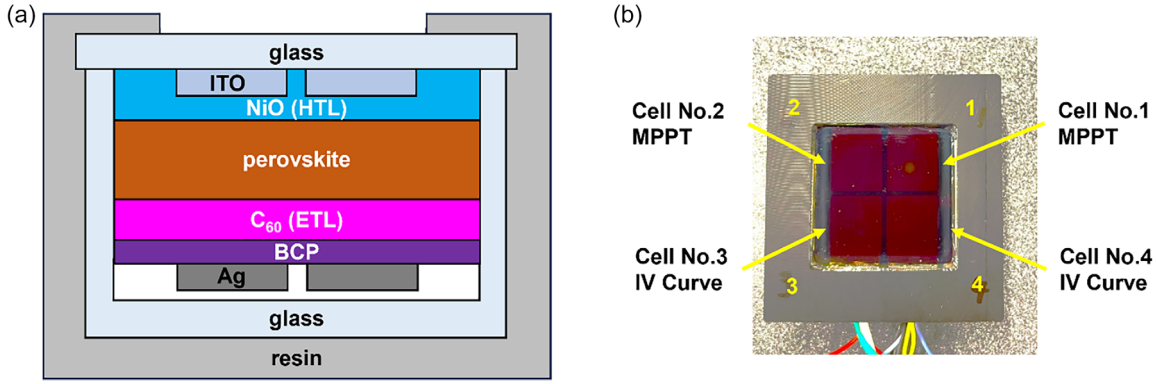


**FIGURE 9** | (a) Schematic and (b) photograph of outdoor-tested PSC samples.

system (EKO Instruments). The incident solar irradiance was measured using a dedicated pyranometer. Performance data were obtained using both the *I–V* curve tracing and MPPT methods. In the *I–V* method, *I–V* sweeps were performed every 2 min between 4:00 and 20:00, with a sweep duration of 1 s, and the device remained in an open-circuit state between the measurements. In contrast, the MPPT method continuously tracked the maximum power point using a hill-climbing algorithm, with *I–V* sweeps conducted at 11:00, 12:00, and 13:00 JST each day; the same sweep duration of 1 s was maintained for both directions. In addition, the solar-cell performance at 12:00 JST on clear days was compared with the daily average efficiency. In addition to standard meteorological data, such as ambient temperature, precipitation, wind speed, and atmospheric pressure, the surface temperature of the encapsulated solar cell was monitored by placing a thermocouple in direct contact with the encapsulant surface. The samples for this outdoor test were installed at a fixed angle of 35° or on a two-axis tracking system, and MPPT control was performed without temperature control in compliance with the ISOS-O O-3 evaluation level.


### Acknowledgments

This work was supported by the Priority Research Project of Tokyo City University, Japan.


### Conflicts of Interest

The authors declare no conflicts of interest.

### Data Availability Statement

The data that support the findings of this study are available from the corresponding author upon reasonable request.

### References


1. T. Miyasaka, A. Kojima, K. Teshima, and Y. Shirai, *Journal of the American Chemical Society* 131 (2009): 6050.

2. N. G. Park, *Materials Today* 18 (2015): 65.

3. M. A. Green, E. D. Dunlop, M. Yoshita, et al., *Progress in Photovoltaics: Research and Applications* 33 (2025): 3.

4. S. Liu, V. P. Biju, *NPG Asia Materials*, 15 (2023): 27, https://doi.org/10.1038/s41427-023-00474-z.

5. K. Miyano, N. Tripathi, M. Yanagida, and Y. Shirai, *Accounts of Chemical Research Journal* 49 (2016): 303.

6. D. B. Khadka, Y. Shirai, M. Yanagida, et al., *Nature Communication* 15 (2024): 882, https://doi.org/10.1038/s41467-024-45228-9.

7. T. Matsui, T. Yamamoto, T. Nishihara, et al., *Advanced Materials* 31 (2019): 1806823, https://doi.org/10.1002/adma.201806823.

8. J. Zhuang, J. Wang, and F. Yan, *Nano-Micro Letters* 15, 2023: 84, https://doi.org/10.1007/s40820-023-01046-0.

9. D. B. Khadka, Y. Shirai, M. Yanagida, and K. Miyano, *ACS Applied Energy Materials* 4 (2021): 11121.

10. D. B. Khadka, M. Yanagida, and Y. Shirai, *Solar Energy Materials and Solar Cells* 281 (2025): 113319, https://doi.org/10.1016/j.solmat.2024.113319.

11. S. Baumann, G. E. Eperon, A. Virtuani, et al., *Energy Environmental Science* 17 (2024): 7566.

12. M. Jošt, B. Lipovšek, B. Glažar, et al., *Advanced Energy Materials* 10 (2020): 2000454, https://doi.org/10.1002/aenm.202000454.

13. M. Konagai, H. Okawa, R. Ishikawa, M. Yanagida, and Y. Shirai, Proc. of the 34th International Photovoltaic Science and Engineering Conf. (PVSEC-34), (2023), 222.

14. V. Paraskeva, M. Norton, A. Livera, et al., *ACS Energy Letters* 9 (2024): 5081.

15. M. Khenkin, H. Köbler, M. Remec, et al., *Energy Environmental Science* 17 (2023): 602.

16. G. Hodes, *Science* 342 (2013), 317, https://doi.org/10.1126/science.1245473.

17. M. Saliba, T. Matsui, K. Domanski, et al., *Science* 2016 (1979): 354.

18. T. Haeger, R. Heiderhoff, and T. Riedl, *Journal of Materials Chemistry C* 8 (2020): 14289.

19. M. Nakamura, I. Takenaka, T. Mabuchi, et al., *ACS Applied Energy Materials* 5 (2022): 10409.

20. M. B. Islam, M. Yanagida, Y. Shirai, Y. Nabetani, and K. Miyano, *ACS Omega* 2 (2017): 2291.

21. L. Cojocaru, S. Uchida, K. Tamaki, et al., *Science Reports* 7 (2017): 1.

22. T. Moot, J. B. Patel, G. McAndrews, et al., *ACS Energy Letters* 6 (2021): 2038.

23. S. Charan, M. Konagai, and K. Takahashi, *Journal of Applied Physics* 50 (1979): 963.

24. J. Mohanraj, B. Samanta, O. Almora, et al., *ACS Applied Material Interfaces* 16 (2024): 42835.

25. S. Zhang, F. Ye, X. Wang, et al., *Science* 380 (2023): 404.

26. R. Nie, Y. Dai, R. Wang, et al., *Nature Communication* 16 (2025): 1.

27. M. Yanagida, T. Nakamura, T. Yoshida, D. B. Khadka, Y. Shirai, and K. Miyano, *Japan Journal of Applied Physics* 62 (2023): SK1054.


### Supporting Information

Additional supporting information can be found online in the Supporting Information section. **Supporting Fig. 1:** Initial PSC performance measured via indoor tests. **Supporting Fig. 2:** Transmittance of the $NiO_x$ layer. **Supporting Fig. 3:** Variations in $R_{sh}$ and $R_s$ of the degraded PSCs. **Supporting Fig. 4:** Comparison of humidity and efficiency degradation. **Supporting Fig. 5:** $V_{oc}$ as a function of surface temperature. **Supporting Fig. 5:** Comparison of the same field of cross-sectional SEM images at different magnifications. **Supporting Fig. 7:** Cross-sectional SEM images (a–c) and OM images (d–f) of dark/open, light/open, and dark/short conditions. **Supporting Fig. 8:** XRD patterns of the outdoor-degraded sample. **Supporting Table 1:** Initial PSC performance parameters.